

Dissolvable Self-Locking Microneedle Patches Integrated with Immunomodulators for Cancer Immunotherapy

Seung-Hwan Joo, Jaehyun Kim, Juhyeong Hong, Shayan Fakhraei Lahiji,* and Yong-Hee Kim*

Advancements in micro-resolution 3D printers have significantly facilitated the development of highly complex mass-producible drug delivery platforms. Conventionally, due to the limitations of micro-milling machineries, dissolvable microneedles (MNs) are mainly fabricated in cone-shaped geometry with limited drug delivery accuracy. Herein, to overcome the limitations of conventional MNs, a novel projection micro-stereolithography 3D printer-based self-locking MN for precise skin insertion, adhesion, and transcutaneous microdose drug delivery is presented. The geometry of self-locking MN consists of a sharp skin-penetrating tip, a wide skin interlocking body, and a narrow base with mechanical supports fabricated over a flexible hydrocolloid patch to improve the accuracy of skin penetration into irregular surfaces. Melanoma, a type of skin cancer, is selected as the model for the investigation of self-locking MNs due to its irregular and uneven surface. In vivo immunotherapy efficacy is evaluated by integrating SD-208, a novel transforming growth factor- β (TGF- β) inhibitor that suppresses the proliferation and metastasis of tumors, and anti-PD-L1 (α PD-L1 Ab), an immune checkpoint inhibitor that induces T cell-mediated tumor cell death, into self-locking MNs and comparing them with intratumoral injection. Evaluation of (α PD-L1 Ab)/SD-208 delivery effectiveness in B16F10 melanoma-bearing mice model confirms significantly improved dose efficacy of self-locking MNs compared with intratumoral injection.

1. Introduction

Advancements in precision 3D printing technologies and materials have dramatically improved prototyping techniques, leading to faster, and more efficient development of biomedical platforms worldwide.^[1] Micro-resolution 3D printers can fabricate highly complex mass-producible parts with improved functionality previously impossible to achieve using micro-milling techniques.^[2] Consequently, the application of micro-scale 3D printing technology in the biomedical field for developing simple and efficient transdermal drug delivery platforms, including microneedles (MNs), has recently attracted increased attention due to its potential to overcome the geometrical limitations of conventional MNs.^[3] Dissolvable MN patches, made of micron-scale polymeric needles, are a patient-friendly transdermal drug delivery system capable of delivering active compounds into the skin with minimal invasiveness.^[4] However, due to their cone-shaped geometry, conventional MNs do not entirely penetrate the skin, resulting in a low delivery accuracy of

loaded cargo,^[5] negatively affecting their clinical application and commercialization in the pharmaceutical field.^[6] Thus, various MN applicators, arrow-head micro-structures, micro-pillar-based MNs, and multi-step fabrication methods have been developed to overcome the limited delivery accuracy of conventional MNs.^[7] However, the fabrication complexity of these approaches has restricted their mass production and application in the pharmaceutical industry. Thus, development of a simple and mass-producible MN platform capable of accurately delivering loaded cargo is urgently needed.

Herein, a digital light processing (DLP) chip-based projection micro-stereolithography 3D printer was used to fabricate a novel self-locking MN capable of complete insertion and locking within the skin tissue, which significantly improved microdose delivery accuracy, overcoming the limitations of conventional MNs. Fabrication simplicity and mass-producibility were primarily focused on during the development of self-locking MN as a highly precise transdermal drug delivery platform. In brief, the self-locking MN geometry was composed of a skin-penetrating sharp tip, a wide skin-locking body, and a narrow base with 4 wide wings providing mechanical support

S.-H. Joo, J. Kim, J. Hong, S. Fakhraei Lahiji, Y.-H. Kim
Department of Bioengineering
Institute for Bioengineering and Biopharmaceutical Research
Hanyang University
Seongdong-gu, Seoul 04763, Republic of Korea
E-mail: lahiji@hanyang.ac.kr; yongheekim@hanyang.ac.kr

S.-H. Joo, J. Kim, J. Hong, Y.-H. Kim
Education and Research Group for Biopharmaceutical Innovation Leader
Hanyang University
Seongdong-gu, Seoul 04763, Republic of Korea
S. Fakhraei Lahiji, Y.-H. Kim
Cursus Bio Inc.
Icure Tower, Gangnam-gu, Seoul 06170, Republic of Korea

 The ORCID identification number(s) for the author(s) of this article can be found under <https://doi.org/10.1002/adma.202209966>.

© 2023 The Authors. Advanced Materials published by Wiley-VCH GmbH. This is an open access article under the terms of the Creative Commons Attribution-NonCommercial-NoDerivs License, which permits use and distribution in any medium, provided the original work is properly cited, the use is non-commercial and no modifications or adaptations are made.

DOI: 10.1002/adma.202209966

for accurate skin insertion. Self-locking MNs were fabricated over a thin, flexible hydrocolloid patch to facilitate their application and adhesion onto irregular skin surfaces. Through a series of in vitro and in vivo evaluations, significantly improved skin insertion, adhesion, and microdose delivery accuracy of self-locking MNs compared with conventional MNs was demonstrated.

Melanoma is a type of skin cancer that typically has an irregular pattern and uneven surface, rendering it a suitable candidate for investigating the adhesion and properties of microdose delivery accuracy of self-locking MNs. Melanoma is a skin cancer caused by mutations in melanocytes, the melanin-producing skin cells,^[8] and the deadliest skin cancer capable of metastasis through lymph nodes and bloodstream to distant organs such as lymph node, lung, liver, bone and brain.^[9] According to the American Cancer Society (ACS), melanoma was the 5th most common type of cancer in 2021, with an estimated 106 110 cases in the US alone. Furthermore, the incidence of melanoma is expected to double and become the 2nd most common cancer by 2040; thus, safe, effective, and patient-friendly platforms that effectively prevent cancer growth and metastasis are urgently needed.^[10] Currently, melanoma treatment approaches are divided based on the melanoma stage.^[11] Immune checkpoint inhibitors blocking programmed cell death-1 (PD-1), programmed cell death ligand-1 (PD-L1), and cytotoxic T lymphocyte antigen-4 (CTLA-4) have shown revolutionary therapeutic effectiveness in melanoma with significant clinical success.^[12] Despite considerable therapeutic advancements, current therapy approaches blocking PD-1 or PD-L1 are limited due to an $\approx 40\%$ objective response rate.^[13] Therefore, to improve the anti-tumor activity of PD-1 or PD-L1 inhibitors, combination therapy of checkpoint inhibitors and immunomodulators has been widely investigated in recent years.^[14]

The transforming growth factor- β (TGF- β) signaling pathway regulates various key cellular processes, including melanoma progression.^[15] TGF- β is a multifunctional cytokine that acts as a tumor suppressor, suppressing cell proliferation, apoptosis, autophagy, inflammation, and angiogenesis in early tumor phases.^[16] However, in later stages of cancer, TGF- β acts as a tumor promoter, enhancing proliferation and epithelial-mesenchymal transition (EMT) of tumor cells, T cell exhaustion and M2 macrophage polarization, leading to metastatic spread within the tumor microenvironment. Recent findings indicate TGF- β inhibition suppresses metastasis and overcomes resistance to immune checkpoint blockade.^[17]

SD-208 is a TGF- β receptor type I (T β RI) kinase inhibitor, capable of increasing T cell activity and anti-metastasis effectiveness against melanoma.^[18] Thus, we hypothesized that combined delivery of anti-PD-L1 (α PD-L1 Ab), allowing T cells to target melanoma, and SD-208, improving melanoma tumor-suppressing effects and T cell activation, would synergistically enhance immunotherapy effectiveness against melanoma.

Melanoma lesions usually are cutaneous, rendering direct drug administration to the tumor microenvironment. Furthermore, tumor-infiltrating lymphocytes (TILs) within the tumor microenvironment secrete cytokines, recruiting effector T cells, which improves the effectiveness of immunotherapy.^[19] Thus, direct delivery of immunotherapeutic agents increases the local immune response while minimizing the systemic side effects.

In the present study, the transcutaneous application of (α PD-L1 Ab)/SD-208 combination therapeutics-loaded self-locking MN patches onto the melanoma tumor site was shown to accurately deliver the microdosage and significantly enhance the anti-tumor effectiveness compared with intratumoral injection. The findings of this study indicated (α PD-L1 Ab)/SD-208-loaded self-locking MN patches can be utilized as an effective minimally invasive patient-friendly immunotherapy approach for patients suffering from stage I to III melanomas.

2. Results and Discussion

2.1. Design and Fabrication of (α PD-L1 Ab)/SD-208-Loaded Self-Locking MN Patches

Accurate microdose transdermal drug delivery plays an essential role in the clinical application of MNs. However, due to the limitations of micro-milling fabrication technologies, conventional MNs are either limited in geometry to cone and pyramid shapes or require a complex multi-step fabrication, casting and precision assembly process (arrow-head MNs, Micro-pillar-based MNs, etc.), limiting their mass-production and pharmaceutical application. Due to advancements in micro-resolution 3D printing technologies, fabrication of highly complex MN geometries capable of remarkably accurate skin penetration, adhesion and microdose delivery of cargo to the target site are now possible. Thus, we combined micro-resolution 3D printing technology and micro-molding techniques to design and fabricate a simple and mass-producible dissolvable self-locking MN platform capable of accurate microdose delivery. In brief, self-locking MN arrays were designed using computer-aided design (CAD) software in 3D, sliced into 2D layers of 10 μ m in height, and transferred to the DLP projection micro-stereolithography-based 3D printer. A 1.5-s flash of ultraviolet (UV) light was projected to the photosensitive resin vat of the 3D printer to photopolymerize each layer of the sliced file, resulting in a highly heterogeneous self-locking MN master mold. Using soft lithography, a widely utilized mold-replicating technique, the master molds were replicated into negative polydimethylsiloxane (PDMS) molds. Dissolvable self-locking MNs were then fabricated by pouring hyaluronic acid (HA) solution containing (α PD-L1 Ab)/SD-208 into the PDMS molds and centrifugation to fill the micro-cavities of the molds (Figure 1A and Figure S1, Supporting Information). The resulting self-locking MNs were fabricated over a thin hydrocolloid patch to enhance the flexibility of the array for application to irregular surfaces. The self-locking MNs were designed with a 30° sharp tip to penetrate the skin with minimum application force, a wide body-to-base ratio to interlock within the skin post-penetration, and four mechanical supports connecting the base and body to avoid needle breakage during the skin insertion process (Figure 1B).

Melanomas with cutaneous nature and irregular surface were selected as the target tumors for evaluating the skin penetration and delivery accuracy of dissolvable self-locking MNs. The majority of recent findings indicated the tumor immune microenvironment can be controlled via the TGF- β signaling pathway. TGF- β -mediated EMT enhances the invasive characteristics of cancer cells while inhibiting the T cell activity

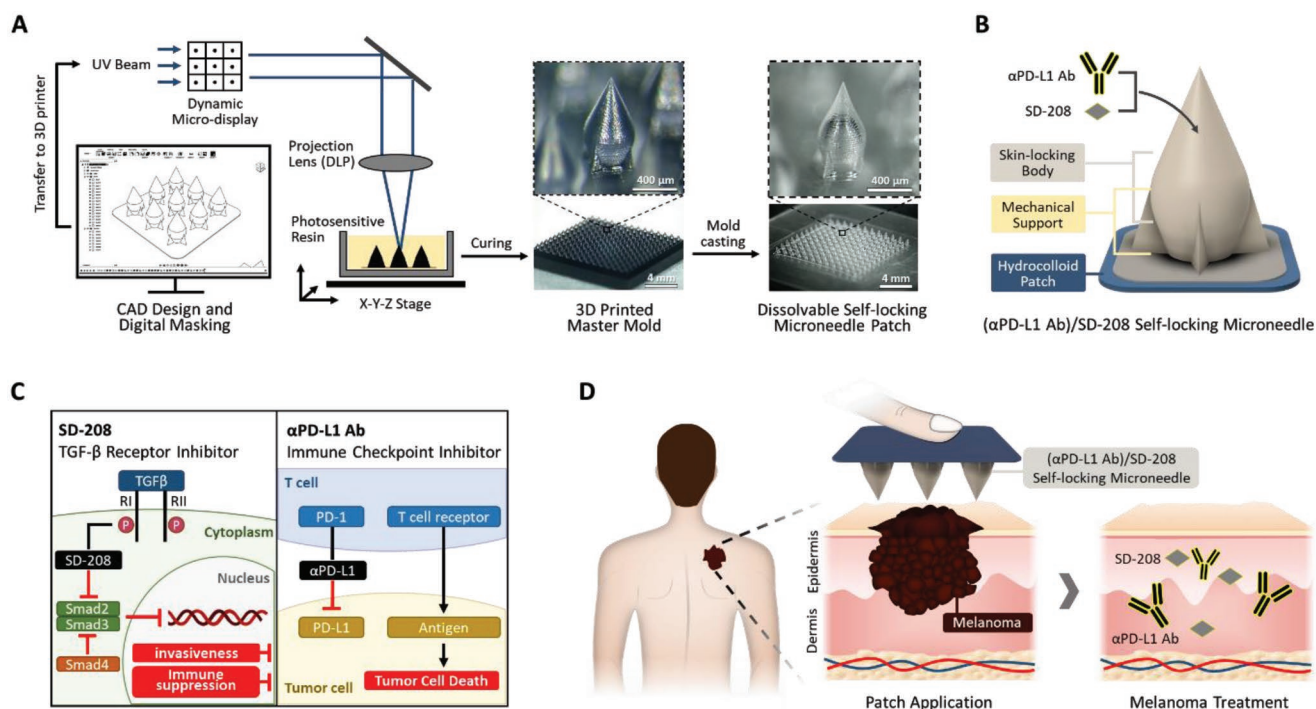


Figure 1. Fabrication of $(\alpha\text{PD-L1 Ab})/\text{SD-208}$ -loaded self-locking MN patches. A) Fabrication process of dissolvable self-locking MN patch using projection micro-stereolithography-based 3D printer combined with micro-molding technique. B) Geometry of $(\alpha\text{PD-L1 Ab})/\text{SD-208}$ -loaded self-locking MN consisting of a sharp, skin penetrating tip, skin-locking wide body, skin penetration mechanical supports and a thin flexible hydrocolloid patch for application onto the irregular skin surface, including melanoma region. C) Mechanism of action in SD-208, a TGF- β receptor inhibitor and $\alpha\text{PD-L1 Ab}$, an immune checkpoint inhibitor, for melanoma combination therapy. D) Schematic illustration of $(\alpha\text{PD-L1 Ab})/\text{SD-208}$ -loaded self-locking MN transcutaneous application onto the melanoma.

within the tumor microenvironment. SD-208 blocks Smad2/3 phosphorylation, Smad3/4-dependent gene transcription and TGF- β target gene expression, resulting in anti-proliferative and anti-metastatic effects, and immunomodulation. Conversely, immune checkpoint inhibitors blocking the interaction between PD-1 and PD-L1 induce T cell-mediated tumor cell death (Figure 1C). Therefore, combination therapy using $(\alpha\text{PD-L1 Ab})/\text{SD-208}$ -loaded self-locking MNs allows T cells to target the melanoma tumor while blocking TGF- β -mediated metastasis and immune suppression, which further enhances anti-tumor effectiveness against the melanoma (Figure 1D).

2.2. Evaluation of Skin Penetration Accuracy of Self-Locking MNs Compared with Cone-Shaped MNs

The geometrical and functional properties of self-locking MNs were compared with conventional cone-shaped MNs designed and fabricated at the same height of 700 μm . **Figure 2A** shows a scanning electron microscope (SEM) image comparison of the most widely used conventional cone-shaped MNs and self-locking MNs. The geometry of conventional cone-shaped MNs consists of a 2- μm sharp tip and a 400- μm -wide base with an even increase in width from top to bottom. However, self-locking MNs consist of a wide body-to-base geometry, in which the width increases from the 2- μm tip to 400- μm mid-body and then decreases as it gets closer to the base at 250 μm . Four thin

wings attached to the mid-body self-locking MN act as mechanical support to avoid accidental breakage or bending during skin insertion.

Mechanical properties of MNs were investigated using a fracture force analyzer to evaluate their skin penetration ability (Figure 2B and Figure S2, Supporting Information). Standard force measurements of self-locking MN confirmed its ability to sustain up to 0.92 ± 0.21 N before bending or breaking. The breakage in self-locking MNs occurred at the lower body, which separated MNs from the base. Therefore, a drop in standard force up to 0.19 ± 0.7 mm displacement was observed before the secondary impact of the load cell on the lower body of the self-locking MN. The mechanical breakage in conventional MNs was 0.83 ± 0.19 N upon 0.36 ± 0.17 mm displacement with no significant difference compared with self-locking MNs (Figure 2C). These results confirmed both MNs had the minimum required force to penetrate the skin as indicated in previous reports.

The concentration distribution of cargo loaded in MNs plays an essential role in enhancing accurate delivery. Rhodamine was used as a drug surrogate to visualize and measure the concentration distribution of each geometry. The 3D reconstruction of Z-stack layers captured from the confocal microscope confirmed that rhodamine was mainly concentrated in the lower body portion of conventional MNs. However, in self-locking MNs, the majority of rhodamine was distributed in the upper portion toward the tip (Figure 2D and Figure S3, Supporting

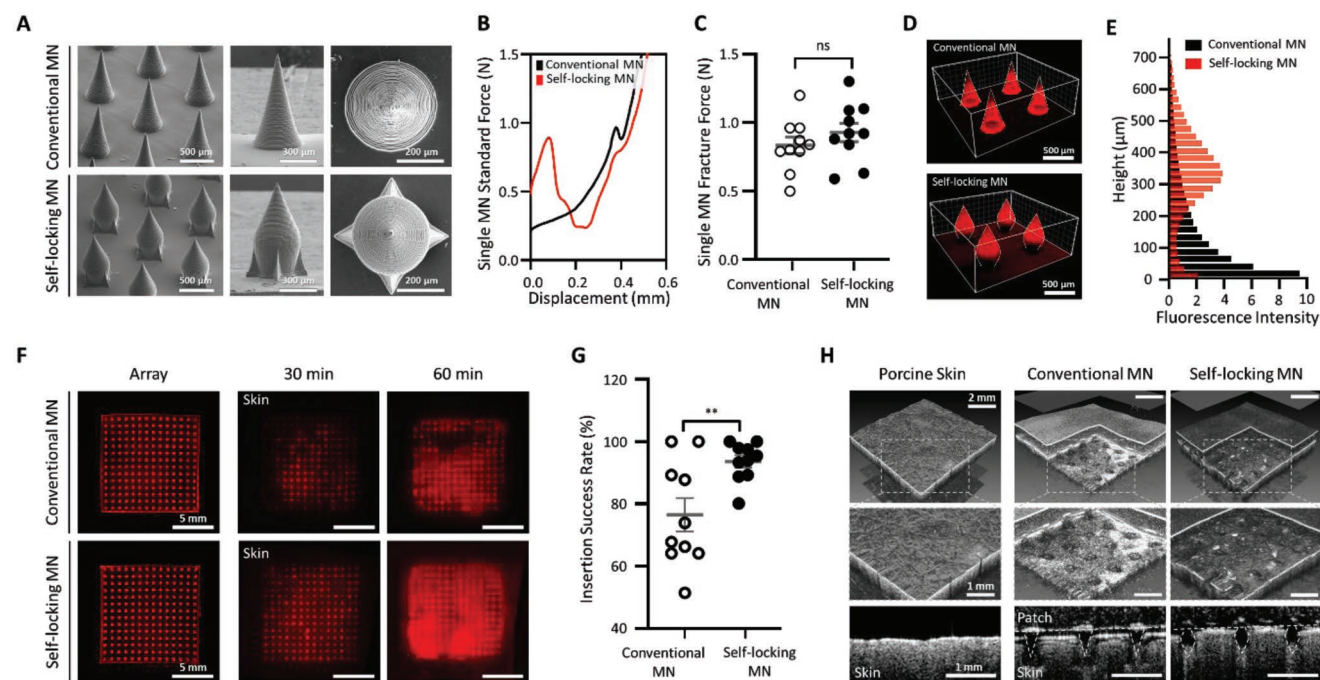


Figure 2. Geometrical advancements of self-locking MNs. A) SEM images of MNs. Right panels show the top view of a single MN. B) Standard force and C) fracture force analysis of single MN ($n = 10$). D) 3D reconstructed images of rhodamine-loaded MNs captured using confocal microscopy. E) Encapsulation distribution of MNs evaluated using fluorescence intensity signal. F) Penetration accuracy evaluation based on application of rhodamine-loaded MNs on pig cadaver skin for 60 min. G) Insertion success rate of MN arrays indicating the percentage of MNs penetrated into the skin on each application ($n = 10$). H) OCT cross-sectional images of MNs showing the penetration pattern and the gap between patch and skin. Data in (C) and (G) are expressed as the mean \pm SEM. ns = not significant, $*p < 0.033$, $**p < 0.002$, $***p < 0.001$, by two-tailed t-test were considered.

Information). Calculation of fluorescence intensity showed the majority of rhodamine distribution ($\approx 80\%$) was concentrated within 0–200 μm in conventional MNs and within 200–700 μm in self-locking MNs (Figure 2E). Due to the risk of incomplete MN insertion, concentrated distribution of cargo in the tip and center is essential to enhance efficient delivery. Therefore, these findings indicated self-locking MNs can deliver loaded cargo with higher accuracy than conventional MNs.

To examine the skin penetration accuracy of MNs, 14×14 arrays of rhodamine-loaded patches were applied onto pig cadaver skin and monitored for up to 60 min. Results showed a consistent pattern of penetration microdots appeared over the skin applied with self-locking MNs; however, in conventional MNs, this pattern was highly irregular (Figure 2F). The number of MNs that successfully penetrated the skin in each type of application showed a significantly higher insertion success rate in self-locking MNs at $93.5 \pm 1.9\%$ compared with conventional MNs at $76.4 \pm 5.2\%$. Furthermore, as shown in Figure 2G, unlike self-locking MNs with a consistent skin insertion success rate, the insertion in conventional MNs was inconsistent in each test. To assess the penetration accuracy of self-locking MNs onto uneven surfaces, we have 3D printed a semi-ellipsoid mass at 5 mm length, 4 mm width, and 2 mm height and covered it with pig cadaver skin to mimic a melanoma tumor model in vitro (Figure S4, Supporting Information). Results indicated a significantly higher insertion success rate in self-locking MNs at $91.6 \pm 4.2\%$ compared with conventional MNs at $59 \pm 7.2\%$. This experiment further supported the potential of self-locking MNs for accurately delivering loaded cargo.

Skin penetration accuracy of MNs was also investigated using optical coherence tomography (OCT), a noninvasive imaging technology to capture cross-sectional images of the skin. Comparison of micro-wounds created upon application of MN arrays showed more prominent openings in conventional MNs than self-locking MNs due to the wider base geometry of conventional MNs (400 μm) compared with self-locking MNs (250 μm , Figure S5, Supporting Information). Microscope-aided measurement of the gap between the MN patch and skin indicated self-locking MN patches were tightly attached to the skin, confirming their skin locking and strong adhesion characteristics (Figure 2H). Altogether, these findings demonstrated the geometry of self-locking MNs significantly enhanced skin penetration and delivery accuracy compared with conventional MNs.

2.3. Evaluation of Skin Adhesion Properties of Self-Locking MNs

MNs were attached to the moving probe of the force analyzer against cadaver skin to evaluate their skin adhesion properties. The probe was displaced downward at a fixed speed of 1 mm min^{-1} to penetrate MNs into the skin, rested for 5 min, and moved upward to detach MNs from the skin. The insertion and extraction patterns were plotted on a graph to evaluate the skin adhesion properties of self-locking MNs compared with conventional MNs. Insertion of MNs into the skin showed a similar pattern and forces of 0.17 ± 0.1 and $0.19 \pm 0.08 \text{ N}$ in both conventional MNs and self-locking MNs, respectively

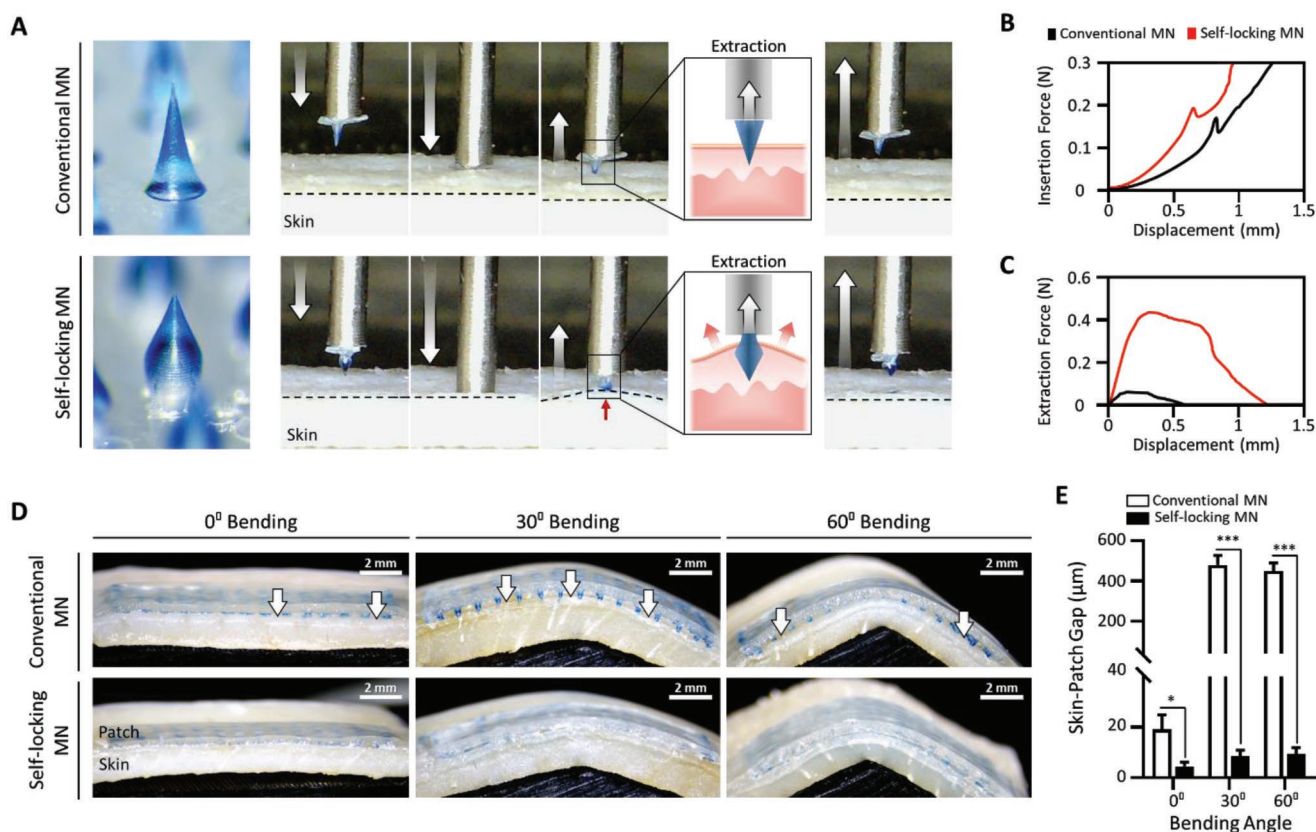


Figure 3. Improved skin adhesion properties of self-locking MNs. A) Microscopic images of MN insertion and extraction from cadaver skin. MNs were attached to the probe of fracture force analyzer and moved down/upward at 1 mm min^{-1} . Blue dye was used to improve the visualization of MNs. Dashed line indicates the surface of the skin. B) Skin insertion and C) extraction forces of MNs. D) Evaluation of 30° and 60° bending effects on the patch-skin gap. MN arrays were applied to the skin and sectioned in half at 5 min post-insertion to measure the patch-skin gap. Arrows indicate the representative points of skin-patch gap. E) Comparison of skin-patch gap affected by increasing the angle ($n = 5$). Data are expressed as the mean \pm SEM. ns = not significant, $*p < 0.033$, $**p < 0.002$, $***p < 0.001$, by two-tailed t -test were considered.

(Figure 3A,B). However, extraction of MNs from the cadaver skin indicated a significantly increased force and elongated displacement in self-locking MNs compared with conventional MNs (Figure 3A,C). Although conventional MNs easily detached from the skin with a minimum force of $0.07 \pm 0.03 \text{ N}$, self-locking MNs interlocked within the skin tissues required a significantly higher force of $0.41 \pm 0.15 \text{ N}$. The displacement was also increased by approximately onefold from 0.51 ± 0.13 to $1.29 \pm 0.38 \text{ mm}$ in conventional MNs and self-locking MNs, respectively.

Next, to further investigate the skin adhesion capability of self-locking MNs, patches were applied to pig cadaver skin and bent up to 60° (Figure 3D). At 0° , the gap was significantly less in self-locking MNs at $4.4 \pm 1.6 \mu\text{m}$ compared with conventional MNs at $19 \pm 5.7 \mu\text{m}$. Upon 30° bending, the gap increased to $477.7 \pm 49 \mu\text{m}$ in conventional MNs but was maintained at $8.4 \pm 2.4 \mu\text{m}$ in self-locking MNs (Figure 3E). Increasing the bending to 60° did not affect the gap between patch and skin in both types of MNs, indicating a remarkably stronger adhesion in self-locking MNs compared with conventional MNs. Collectively, these findings confirmed that self-locking MNs could significantly enhance dynamic skin adhesion and further improve delivery accuracy during the backbone dissolution process.

2.4. Investigation of Cutaneous Permeation Kinetics of Self-Locking MNs In Vitro

Self-locking MNs and conventional MNs were loaded with rhodamine and applied onto cadaver skin placed over a Franz cell diffusion to evaluate the cutaneous permeation kinetics. The Franz cell diffusion was designed to mimic the biological environment of the human body in vitro. The release profile of self-locking MNs showed a significantly higher cargo transport at 4 h post-application ($51.3 \pm 5.6\%$) compared with conventional MNs ($28.3 \pm 4.2\%$). At 24 h, the cumulative release amount was increased up to $79.3 \pm 5.6\%$ in self-locking MNs compared with conventional MNs $50.3 \pm 7.6\%$ (Figure 4A). The MN residue on patches at 1 h post-application confirmed self-locking MNs were entirely dissolved; however, a majority of the base portion in conventional MNs remained on the patch (Figure 4B). The images were taken using an optical microscope equipped with a fluorescence detection lens, which resulted in baseline reflection and increased intensity of the light in the lower section of MNs. As shown in Figure 2E, the majority of cargo was distributed in the lower half of conventional MNs, further confirming their lower permeation efficiency than self-locking MNs. These findings further highlighted the effects of self-locking MN geometry in improving microdose delivery accuracy of loaded cargo.

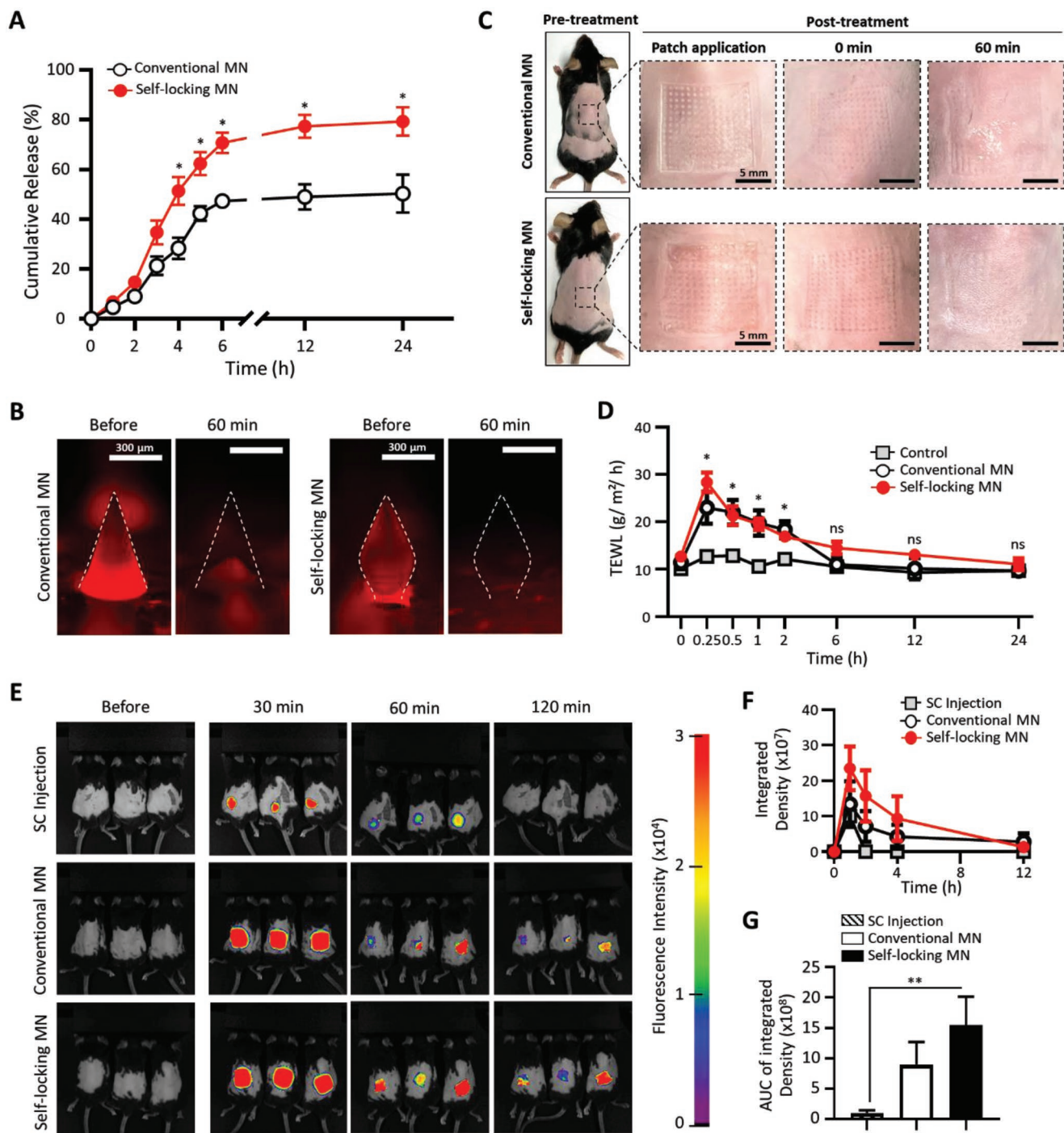


Figure 4. Cutaneous permeation kinetics of self-locking MNs. A) Comparison of cutaneous permeation kinetics of self-locking MNs and conventional MNs using Franz cell diffusion ($n = 3$). Data are expressed as the mean \pm SEM. ns = not significant, $*p < 0.033$, $**p < 0.002$, $***p < 0.001$, by two-tailed t -test were considered. B) Dissolution pattern of MNs at 60 min post-application onto cadaver skin. C) Applying MNs onto mice created micro-wounds at 0 min that were partially healed at 60 min post-application. D) TEWL analysis of vapor flux in mice up to 24 h post-MN application ($n = 4$). E) Fluorescence intensity detected using IVIS up to 120 min post-application. F) Integrated density of fluorescence intensity up to 12 h post-application ($n = 3$). G) Area under curve (AUC) comparison of 0–12 h fluorescence intensity in the subcutaneously injected mice and MN patches ($n = 3$). Data are expressed as the mean \pm SEM. ns = not significant, $*p < 0.033$, $**p < 0.002$, $***p < 0.001$, by one-way ANOVA with Tukey's post hoc test were considered.

Generally, insertion of MNs into the skin creates micro-wounds, leading to disruption of the barrier properties of the skin, skin irritation, and increased risk of body exposure to

pathogens. Therefore, ensuring micro-wounds are healed and skin barrier properties are recovered after MN application is necessary. To evaluate the effects of MNs on the barrier

function of the skin, the transepidermal water loss (TEWL) of mice skin was measured for up to 24 h. Application of MN patches onto the dorsal area of mice created a pattern of micro-wounds at 0 min that partially faded in mice treated with both types of MNs at 60 min post-application (Figure 4C). Insertion of self-locking MNs and conventional MNs significantly increased the vapor flux and TEWL levels to 28.3 ± 2 and $22.9 \pm 3.3 \text{ g m}^{-2} \text{ h}^{-1}$, respectively. TEWL was then reduced to normal levels at 6 h post-application, with no significant difference from the control group (Figure 4D). Altogether, TEWL results suggested restoration of skin barrier properties from 6 h post-MN application, regardless of MN geometry. These findings confirmed the micro-wounds created upon insertion of MN patches were entirely healed after 6 h. HA accelerates the wound healing process; thus, use of HA as the MN backbone matrix could have further enhanced the micro-wound healing process.

Next, to examine the transcutaneous localization and release pattern of MNs, subcutaneously injected rhodamine was compared with MN patches using in vivo imaging system (IVIS) for up to 60 min (Figure 4E). The fluorescence intensity of subcutaneously injected rhodamine was initially increased up to $10 \times 10^7 \pm 3.4 \times 10^7$ with subcutaneous injection, to $13.3 \times 10^7 \pm 6.4 \times 10^7$ with conventional MNs, and to $23.5 \times 10^7 \pm 6.1 \times 10^7$ in self-locking MN-treated mice. At 120 min post-application, rhodamine in the subcutaneously injected mice was significantly reduced to undetectable levels; however, levels were $7.1 \times 10^7 \pm 4.3 \times 10^7$ in conventional MN-treated and $15.7 \times 10^7 \pm 7.2 \times 10^7$ in self-locking MN-treated mice, indicating accurate microdose delivery and improved localization of loaded cargo (Figure 4F). Next, to quantify and compare the localization and sustained permeation pattern of subcutaneous injection compared with MN patches, the total integrated density of fluorescence intensity during 12 h of application was measured. Results indicated a significantly higher localization in the self-locking MN-treated mice ($15.4 \times 10^8 \pm 4.6 \times 10^8$) compared with the subcutaneously injected mice ($1 \times 10^8 \pm 0.4 \times 10^8$; Figure 4G). Altogether, these findings confirmed improved microdose delivery accuracy, slower permeation, and increased localization of loaded cargo within MNs compared with subcutaneous injection. Thus, we hypothesized that sustained release and localization of (α PD-L1 Ab)/SD-208 at cutaneous melanoma lesions would further enhance immunomodulatory effectiveness.

2.5. Anti-Proliferative and EMT-Inhibiting Effects of SD-208 in B16F10 Melanoma Cells

SD-208, an inhibitor of TGF- β receptor I (TGF- β RI) kinase, was used as combination therapy with α PD-L1 Ab to confirm its therapeutic effects on melanoma. In a majority of studies, TGF- β was suggested to promote proliferation of cancer cells and metastasis via EMT^[20] (Figure S6, Supporting Information). Thus, the morphological changes and growth rate of B16F10 cells affected by TGF- β were analyzed based on a series of in vitro evaluations.

First, immunofluorescence analysis was conducted using anti-tubulin antibodies to evaluate the morphological change

of B16F10 cells (Figure 5A and Figure S7, Supporting Information). Because tubulin is a structural element in the cytoskeleton of cells, TGF- β treatment elongates the tubulin into an invasive fibroblast type.^[21] However, SD-208 normalized the morphology of the melanoma cancer cells to epithelial type with shortened ends. To verify the morphological change was caused by inhibition of Smad3, a core transcription factor involved in the TGF- β signaling pathway, the expression levels of Smad3 and p-Smad3 were measured in B16F10 cells using immunoblotting assay (Figure 5B). Results confirmed TGF- β treatment significantly increased p-Smad3 expression (activated forms of Smad3); however, co-treatment with SD-208 inhibited Smad3 phosphorylation, indicating successful blockade of TGF- β signaling in B16F10 cells. Furthermore, TGF- β and SD-208 treatments altered E-cadherin and N-cadherin expression levels. N-cadherin, highly expressed during invasive TGF- β -induced cell transformation, was significantly downregulated in the SD-208-treated cells, resulting in normalized E-cadherin levels. These findings confirmed that SD-208 successfully interfered with Smad3 phosphorylation and normalized TGF- β -induced E-cadherin and N-cadherin levels.

N-cadherin, upregulated by TGF- β , increases the invasiveness of cancer cells, induces sporadic morphology, cell migration, and extracellular matrix infiltration.^[22] To demonstrate the anti-migration and anti-invasion effects of SD-208 via TGF- β inhibition, a wound healing assay and a spheroid assay against B16F10 cells were conducted. The wound-healing assay was performed by scratching B16F10-seeded well plates and the TGF- β -facilitated wound closure observed. The scratched area was significantly reduced after 20 h post-TGF- β treatment ($65.2 \pm 16.1\%$) with a 1.8-fold increased wound closure rate compared with the untreated B16F10 cells indicated as control group ($35 \pm 7.07\%$). In contrast, the SD-208-treated cells showed a wound closure rate ($30.2\% \pm 6.6\%$) similar to the control (Figure 5C,D). These results verified the cell migration rate was affected by N-cadherin protein expression. Thus, because TGF- β stimulates cancer cell mobility, downregulation of TGF- β in the tumor environment can inhibit tumor metastasis.

TGF- β disturbs interactions between cell–cell anchoring proteins (E-cadherin) and stimulates the invasiveness of cancer cells.^[23] Thus, cells are loosened from the tumor and separated from the primary tissue area. E-cadherin plays an essential role in forming and maintaining intercellular adhesion, cell junctions, and spheroid compaction.^[24] To confirm the TGF- β -related weakening of intercellular adhesion in a 3D environment, 3D-culture spheroids of B16F10 cells were induced with TGF- β (5 ng mL^{-1} ; Figure 5E). Formation of compact spheroids was mediated by high E-cadherin interactions; however, TGF- β induction during EMT decreased E-cadherin levels and ruptured spheroids.^[25] Consequently, the spheroids treated only with TGF- β showed loose tight junctions and growth of the core area was diminished after the 6th day. However, the effects of TGF- β were suppressed, and spheroids maintained their interaction in the SD-208-treated cells (Figure 5F). Taken together, these results indicated that inhibiting TGF- β in tumor sites using SD-208 can reduce the invasiveness of cancer cells and inhibit severe metastasis. Thus, SD-208 was used as a combination therapy agent with α PD-L1 Ab to further improve the immunotherapy effectiveness against melanomas.

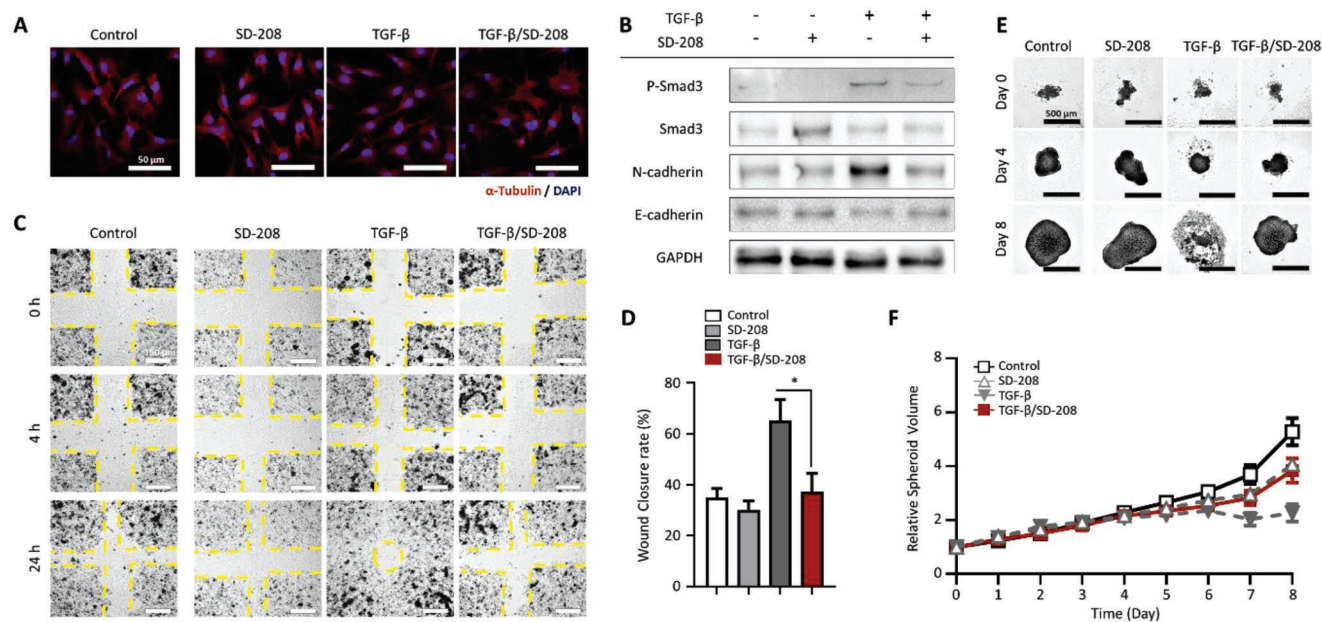


Figure 5. Anti-proliferative and anti-EMT effects of SD-208 in B16F10 cancer cells. A) Morphological differentiation of B16F10 cancer cells after 24 h of TGF- β and SD-208 treatment. B) Protein level analysis of E-cadherin and N-cadherin based on immunoblotting. B16F10 cancer cells were pre-treated with SD-208 (1 μ M) for 24 h and exposed to TGF- β (5 ng mL⁻¹). C) Wound healing assay images of B16F10 cell migration at 0, 4, and 24 h of treatment. D) Wound closure rate analysis of the treated cells. The data were normalized to the wound area at 0 h ($n = 4$). Data are expressed as the mean \pm SEM. ns = not significant, * $p < 0.033$, ** $p < 0.002$, *** $p < 0.001$, by one-way ANOVA with Tukey's post hoc test were considered. E) Representative 3D-culture spheroid images of B16F10 cells. F) Relative spheroid growth was calculated by measuring the spheroid area and normalized to the initial spheroid size at day 0 ($n = 8$).

In numerous studies TGF- β was shown to promote T cell suppression by inducing the PD-L1 expression in cancer cells.^[26] Overexpressed PD-L1 expression inhibits the T cell receptor (TCR) signaling pathway by binding to the PD-L1 receptor (PD-1) on CD8⁺ T cells, resulting in the exhaustion of cytotoxic T cells.^[27] Our findings confirmed that SD-208 ameliorated PD-L1 expression in B16F10 cells activated by TGF- β (Figure S8, Supporting Information). Therefore, the combination of SD-208 and immune checkpoint blockade antibody α PD-L1 Ab loaded into self-locking MNs would synergistically lower the PD-L1 expression in cancer cells and improve the effectiveness of α PD-L1 Ab against PD-L1.

2.6. Anti-Tumoral and Immunomodulation Efficacies of (α PD-L1 Ab)/SD-208-Loaded Self-Locking MN in Orthotopic Melanoma Mouse Model

The most common characteristic of melanoma is its asymmetrical and uneven brown bumpy spots continuously changing in size and shape.^[28] Thus, utilizing a transdermal drug delivery platform capable of firmly interlocking within the skin tissue on the tumor site to accurately deliver melanoma-treating agents is essential. As shown in the earlier sections, self-locking MNs, fabricated over a flexible hydrocolloid patch, were capable of strong adhesion and interlocking within dynamic tissues with irregular surfaces, rendering application to cutaneous melanoma lesions suitable.

To evaluate the combination therapy efficacy of SD-208 and α PD-L1 Ab in melanomas, an orthotopic B16F10 melanoma

mouse model was constructed. The melanoma-bearing mouse model was established via subcutaneous injection of B16F10 cells (2×10^5) to the dorsal flank of C57BL/6 mice. On the 8th day of modeling, the mice were treated with (α PD-L1 Ab)/SD-208-loaded self-locking MNs ((α PD-L1 Ab)/SD-208 SLMNs), blank self-locking MNs (HA SLMNs), SD-208-loaded self-locking MNs (SD-208 SLMNs), α PD-L1 Ab-loaded self-locking MNs (α PD-L1 Ab SLMNs), α PD-L1 Ab/SD-208 intratumoral injection ((α PD-L1 Ab)/SD-208 IT), or PBS intratumoral injection (PBS IT; Figure 6A and Figures S9–S11, Supporting Information). At day 18 post-treatment, the (α PD-L1 Ab)/SD-208 SLMN-treated mice showed the slowest tumor growth at 384.06 ± 88.63 mm³ than all other treated mice with a significant difference of $\approx 60\%$ compared with the PBS IT-injected mice (966.81 ± 156.63 mm³; Figure 6B). Although both MN-treated and intratumorally injected mice were administered the same volume of (α PD-L1 Ab)/SD-208, the prolonged release of agents at the tumor site may have further improved the immunotherapy efficacy of self-locking MNs compared with intratumoral injection. Furthermore, measurement of harvested tumors on day 18 showed a significant decrease in tumor size and weight in (α PD-L1 Ab)/SD-208 SLMN (0.07 ± 0.01 g)- and (α PD-L1 Ab)/SD-208 IT (0.14 ± 0.04 g)-treated mice compared with HA SLMN (0.37 ± 0.08 g)-, SD-208 SLMN (0.27 ± 0.07 g)- and α PD-L1 Ab SLMN (0.25 ± 0.03 g)-treated, and PBS IT (0.54 ± 0.03 g)-injected mice (Figure 6C,D). Although the difference in tumor weight between self-locking MNs and intratumorally injected mice was insignificant, the (α PD-L1 Ab)/SD-208 SLMN-treated mice showed significantly higher effectiveness in inhibiting the tumor growth volume for up to

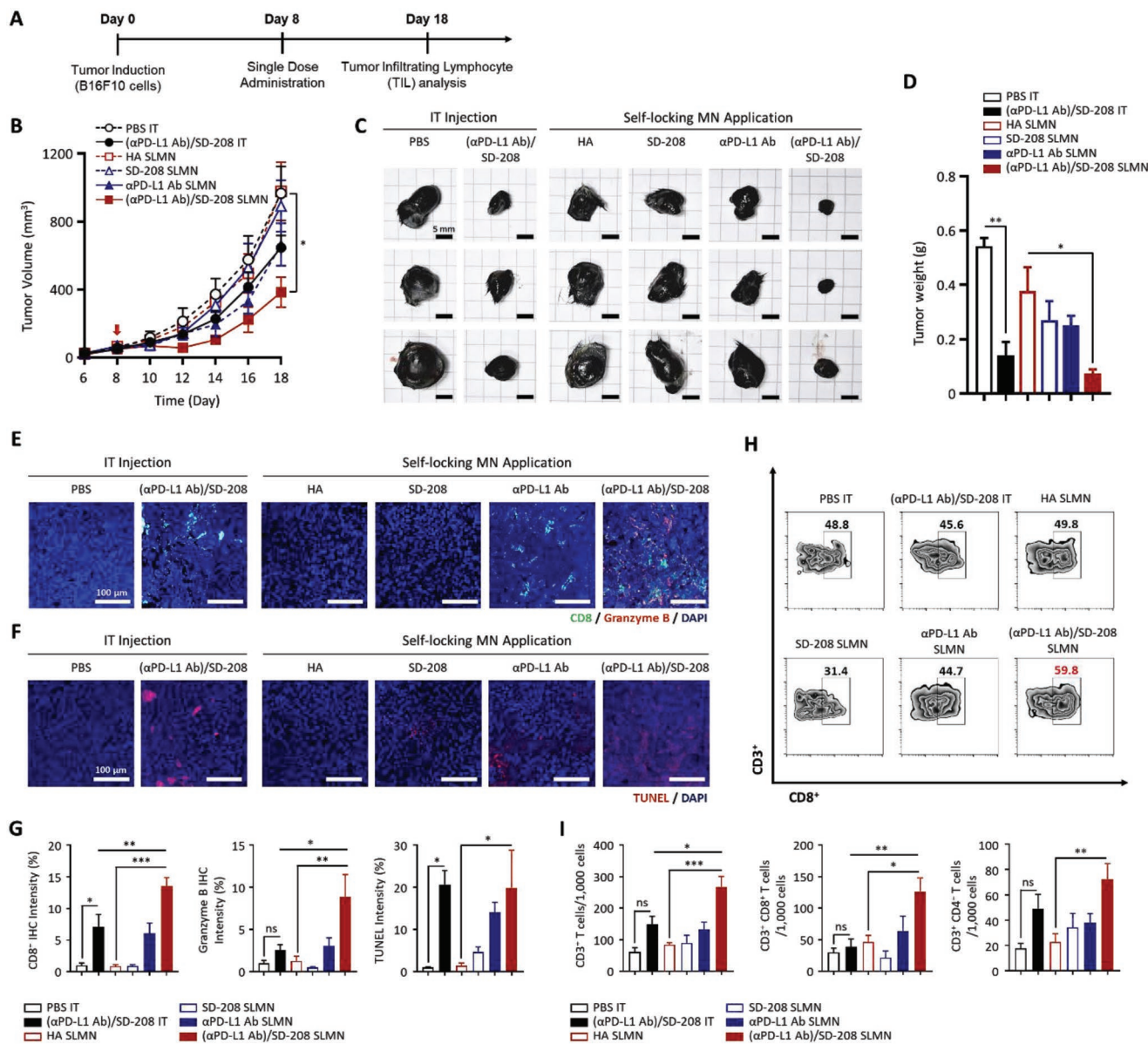


Figure 6. Anti-tumoral and immunomodulation efficacies of (αPD-L1 Ab)/SD-208 SLMNs in orthotopic melanoma mouse model. A) Timeline overview of treatment and evaluation of C57BL/6 melanoma mouse model inoculated with B16F10 cells. B) The tumor volume measurement for 18 days post-treatment ($n = 5$). C) Representative images of tumors harvested on the 18th day and D) tumor weight measurements ($n = 3$). E) Immunofluorescent staining in tumor sections. The green signals indicate the CD8⁺ cells. The red signals indicate granzyme B⁺ cells. F) TUNEL assay in tumor sections. The red signals indicate TUNEL⁺ cells. G) The ratio of positive fluorescence intensity in immunofluorescent staining and TUNEL assay. The intensity in each type of application was normalized to the intensity of PBS ($n = 5$). H) Representative plots of CD3⁺ and CD8⁺ T cells in tumor tissues analyzed using flow cytometry. I) Total tumor tissue was harvested and stained for anti-CD3, anti-CD4, and anti-CD8 antibodies ($n = 5$). The ratio of CD3⁺ T cells, CD3⁺CD8⁺ T cells, and CD3⁺CD4⁺ T cells in 1×10^4 cells was measured using flow cytometric analysis. Data are expressed as the mean \pm SEM. ns = not significant, * $p < 0.033$, ** $p < 0.002$, *** $p < 0.001$, by one-way ANOVA with Tukey's post hoc test were considered.

18 days. Further evaluations of survival rates in melanoma-bearing mice confirmed the improved anti-tumoral therapeutic effectiveness of (αPD-L1 Ab)/SD-208 SLMNs compared with intratumoral injection. In addition, the histological analysis of mice organs in all treated mice indicated the safety of (αPD-L1 Ab)/SD-208 in treating melanomas.

Granzyme B⁺, expressed by CD8⁺ T cells, is a mediator of immunity against tumor cells.^[29] Thus, to evaluate the immunomodulation efficacy of (αPD-L1 Ab)/SD-208 SLMNs, the

expression levels of CD8⁺ and granzyme B were assessed. Results indicated a significantly increased fluorescence intensity in (αPD-L1 Ab)/SD-208 SLMN-treated mice, highlighting its immunomodulation effectiveness against tumors (Figure 6E and Figure S12, Supporting Information). The intensity of CD8⁺ fluorescence in (αPD-L1 Ab)/SD-208 SLMN-treated mice (13.52 ± 1.35) was increased by approximately 14-fold compared with PBS IT-injected mice (1.0 ± 0.38) and two-fold compared with (αPD-L1 Ab)/SD-208 IT-injected mice

(7.10 ± 1.9). Furthermore, the intensity of granzyme B fluorescence in (α PD-L1 Ab)/SD-208 MN-treated mice (8.87 ± 5.93) was increased by approximately ninefold compared with PBS IT-injected mice (1.0 ± 0.76) and 3.5-fold in (α PD-L1 Ab)/SD-208 IT-treated mice (2.54 ± 1.49 ; Figure 6G). CD8⁺ T cells are immune cells targeting cancer via immunosuppression within the tumor microenvironment.^[30] Our findings indicated a significantly increased intensity of TUNEL staining used to detect apoptotic cells in the (α PD-L1 Ab)/SD-208 SLMN-treated mice, indicating the increased CD8⁺ T cell activation in tumor sites had successfully triggered the apoptosis of cancer cells (Figure 6F,G and Figure S13, Supporting Information). Immunofluorescence evaluation of the tumor tissues indicated cytotoxic T cells were increased and their activity was the primary factor in tumor suppression as shown in (α PD-L1 Ab)/SD-208 SLMN-treated mice.

To quantify the infiltrated cytotoxic T cells in the tumor, tumor-infiltrating lymphocytes (TILs) were analyzed using flow cytometric analysis with specific antibodies. We analyzed 10 000 cells in tumor tissue and identified T lymphocytes, cytotoxic T cells and helper T cells using CD3⁺, CD8⁺ and CD4⁺ markers, respectively (Figure 6H,I). CD3⁺ signal, a component of the T-cell receptor (TCR) on lymphocytes, was significantly increased in the (α PD-L1 Ab)/SD-208 SLMN-treated mice compared with the intratumorally injected mice. Furthermore, the proportion of CD8⁺ cytotoxic T cells was highest in (α PD-L1 Ab)/SD-208 SLMN-treated mice, larger than in all other treated mice, indicating greater T cell-mediated anti-tumoral effects. In addition, CD4⁺ T cells, helper T cells that contribute to anti-tumoral effects by activating other cytotoxic T cells, were also significantly increased in the (α PD-L1 Ab)/SD-208 SLMN-treated mice compared with all other mice. Therefore, we confirmed that numerous cytotoxic T cells exist in tumors and several helper T cells aid in activating the immune response.

Consequently, the local inhibition of TGF- β and α PD-L1 Ab resulted in improved immunomodulation, confirmed based on improvement in the recruitment and activity of T cells. (α PD-L1 Ab)/SD-208 SLMNs exerted an anti-tumor effect with an expanded TIL synergistic effect of blocking TGF- β and immune checkpoints in the C57BL/6 melanoma mouse model. Combination therapy of α PD-L1 Ab and SD-208-loaded self-interlocking MNs showed a sufficient immune response in activating T cells for killing melanoma cells in the C57BL/6 model. Because activation of TILs caused by self-locking MNs was more effective in improving immune activity compared with intratumoral injection, we hypothesized (α PD-L1 Ab)/SD-208 SLMNs would have a high potential to be utilized as a patient-friendly, minimally invasive, and effective alternative to injection.

3. Conclusion

During the past decades, the potential of MNs as a promising transdermal drug delivery platform for micro- and macro-biomolecules has been suggested in numerous studies. Compared with oral administration and hypodermic injection, MNs are advantageous because they bypass the first-pass metabolism

of the gastrointestinal tract with oral administration and avoid pain, blood-borne infection, and patient discomfort associated with hypodermic injection. Furthermore, the sustained release characteristic of MNs has been reported to improve dose efficiency compared with subcutaneous immunization. However, due to the elastic properties of the skin, the penetration and delivery accuracy of conventional MNs are limited. Thus, a wide range of MN applicators and secondary structures, including micro-pillars, were developed to improve the delivery accuracy of MNs for clinical applications. However, the complexity of these approaches has limited their clinical application and commercialization.

In the present study, a micro-resolution DLP-based projection micro-stereolithography 3D printer was used to fabricate a novel MN geometry capable of accurate skin insertion, adhesion, and microdose delivery of loaded cargo. The self-locking MNs consisted of a sharp tip and wide body-to-base geometry, which holds them firmly within the skin post-insertion. In brief, self-locking MN molds were designed in 3D using CAD, sliced into 2D layers, and 3D printed with a high precision of 10 μ m. The printed master molds were then replicated using soft lithography technique into PDMS negative molds to fabricate dissolvable self-locking MN patches. Soft lithography technique is a simple and cost-effective approach for the mass production of self-locking MNs, facilitating their clinical application and commercialization.

In vitro evaluation of skin penetration and permeation showed a significantly improved efficiency of self-locking MNs compared with conventional MNs. The distribution concentration of MN-loaded cargo within the tip section increased delivery accuracy. Based on 3D reconstruction of confocal images, $\approx 80\%$ of compounds were loaded within the base of conventional MNs, which dramatically reduced the delivery accuracy. However, in self-locking MNs, the majority of cargo was distributed within the upper section toward the tip, significantly increasing delivery accuracy. OCT cross-sectional images also confirmed a tighter patch-to-skin adhesion in self-locking MNs. Dynamic skin bending test at 0° to 60° further supported the significantly improved skin adhesion properties of self-locking MNs compared with conventional MNs.

Due to the irregular and uneven surface characteristics, melanomas were selected as a model to evaluate skin adhesion and delivery accuracy of self-locking MNs. Monotherapy using α PD-L1 Ab showed the most therapeutic effect in clinical studies, with a 40% objective response rate in stage IV melanoma patients. Therefore, to further improve the immunotherapy efficiency of patients suffering from stage I to IV melanoma, α PD-L1 Ab was integrated with SD-208 into a single platform as a combination therapy to suppress metastasis and resistance against immune checkpoint blockade and the effectiveness against melanoma evaluated in B16F10 tumor-bearing mouse model. Comparison of tumor volume, weight, immunomodulation level, and the number of infiltrated cytotoxic T cells indicated a single dose of combination therapy with (α PD-L1 Ab)/SD-208 was significantly more effective in treating melanoma than monotherapy with either α PD-L1 Ab or SD-208. Furthermore, (α PD-L1 Ab)/SD-208-loaded self-locking MNs showed considerably greater efficiency in treating melanomas than intratumoral injection. Although both MN-treated

and intratumorally injected mice were administered the same volume of (α PD-L1 Ab)/SD-208, the improved melanoma treatment effectiveness in self-locking MNs was likely caused by accurate microdose delivery and sustained localized diffusion of cargo from the HA backbone matrix.

In conclusion, the self-locking MNs created in the present study demonstrated to significantly improve microdose delivery efficiency of loaded cargo compared with conventional MNs with significantly higher immunomodulation effectiveness compared with intratumoral injection. The minimally invasive nature, fabrication simplicity, economical mass-producibility and improved microdose delivery accuracy of self-locking MNs indicate their significant potential as an alternative drug delivery platform for conventional MNs, oral administration and hypodermic injections for clinical application. Using minimally invasive painless self-locking MNs as an alternative to repeated painful injections in patients can effectively control their disease while improving their quality of life. Loading active agents into MNs can further enhance their storage stability, reduce the requirement for cold-chain transportation, and expand the range of treatment coverage worldwide. Thus, the real-life application of self-locking MNs in pharmaceuticals and vaccine delivery can provide the basis for overcoming various social and economic obstacles.

4. Experimental Section

Reagents: Sodium hyaluronate (HA) was purchased from Bloomage BioTechnology Corporation Limited (Jinan, China). Recombinant mouse TGF- β 1 protein (TGF- β) was purchased from R&D Systems (Minnesota, USA). 2-(5-chloro-2-fluorophenyl)pteridin-4-yl]pyridin-4-yl-amine (SD-208), dimethyl sulfoxide (DMSO), rhodamine B, fluorescein-5-isothiocyanate (FITC), Cell Counting Kit-8 (CCK-8), and red blood cell lysis buffer were purchased from Sigma-Aldrich (St. Louis, USA). InVivoMAb anti-mouse PD-L1 (α PD-L1 Ab) was acquired from Bio X Cell (Lebanon, USA). Penicillin streptomycin, and fetal bovine serum (FBS) were purchased from Gibco (New York, USA). Dulbecco's modified Eagle's medium (DMEM), Dulbecco's phosphate-buffered saline (DPBS), and trypsin were purchased from WELGENE (Seoul, Korea). DNase 1 solution and collagenase/hyaluronidase were obtained from STEMCELL Technologies (Vancouver, Canada). Mouse anti-CD3, CD4, and CD8 antibodies were purchased from BioLegend (San Diego, USA). Cyanine 5.5 NHS ester (Cy 5.5) was purchased from Lumiprobe (Wan Chai, Hong Kong).

Fabrication of Dissolvable MNs: MNs were designed using Autodesk Fusion CAD software in 3D and sliced into 2D layers for fabrication with the Projection MICROARCH S140 3D printer (Boston Microfabrication, Massachusetts, USA) in 14×14 arrays. HTL, a high-performance silicone castable resin with a heat deflection temperature (HDT) of 114°C and glass transition temperature (T_g) of 172°C , was employed as the backbone resin for the 3D printing of MN molds. The 3D printed molds were then replicated using soft lithography with polydimethylsiloxane (PDMS, SYLGARD 184 Silicone Elastomer, DOW Corning, Michigan, USA) at a 10:1 ratio to fabricate negative molds. Polymer solutions were prepared by mixing 20% (w/v) HA in PBS and DMSO at a 9:1 ratio. The tensile strength of HTL resin was 71.5 MPa, which is suitable for the continuous silicone casting process. Using the mold casting method, both conventional and self-locking dissolvable MNs were fabricated by pouring 65 μL of exact same solutions and centrifuging at 3,000 rpm for 5 min. The MNs were placed at 4°C for 12 h to solidify prior to application. An adhesive dressing patch made of hydrocolloid material was purchased from Cosmax I cure Inc. (Seongnam-si, Korea) to detach dissolving MNs from PDMS molds.

Characterization: The microscopic morphology of the MNs was characterized using Apreo S Hivac SEM (FEI Company, Eindhoven, the Netherlands). Individual MNs were mounted onto metal stubs with double-sided carbon tape and coated with platinum. Fluorescence distribution in the MNs was captured with the STELLARIS 8 STED Confocal Laser Scanning Microscopy (Leica Microsystems, Wetzlar, Germany). Microscopic images were recorded using a KCS-2000SS microscope (OPTINITY, Seongnam-si, Korea).

Measurement of Fracture and Skin Penetration Forces: The axial load fracture force of each MN and the force required to penetrate the skin were measured using the Zwick Roell Z0.5 Materials Testing Machine (ZwickRoell, Ulm, Germany). Each MN was placed on the aluminum plate with the needle tip facing upward. The force was applied against the tip of the MN at a constant speed of 10 mm min^{-1} at the pre-load point. The material-testing machine recorded the distance and force until the preset force 1.5 N was achieved.

Ex-Vivo Cutaneous Permeation Kinetics of MNs: Cumulative release studies were conducted using Franz cell diffusion. The diffusion system was equipped with an inlet and outlet attached to a thermostatic water-circulator bath. Receiver chambers were filled with PBS at $32 \pm 1^\circ\text{C}$ for 24 h. MNs were applied on pig cadaver skin (APURES, Pyeongtaek-si, Korea) placed over each cell for 1 h. The solution from the chamber was collected at 0, 1, 2, 3, 4, 5, 6, 12, and 24 h. Rhodamine B content was quantitated using INFINITE 200 PRO microplate reader (TECAN, Zurich, Switzerland).

Skin Penetration Analysis Based on OCT: The skin penetration ability of the MNs was analyzed using OCT (Kyungpook National University, Daegu, Korea). MNs were applied to pig cadaver skin and real-time layer-by-layer recording was performed. The layers were then combined and reconstructed into a single image.

Fluorescence Distribution Analysis: The dorsal hair of C57BL/6 mice was shaved 24 h prior to the experiment. Same volume of 65 μL of 0.01% (w/v) rhodamine B-loaded MNs and SC injection solutions were applied to the dorsal site of mice for 1 h and wiped gently using a cotton swab. In vivo biodistribution of rhodamine B-loaded MNs was quantified using an in vivo imaging system (FOBI IVIS, CELLGENTEK, Deajeon-si, Korea) for up to 12 h. Fluorescent images were taken using diffuse-type LED in red light channel (630 nm) at fixed settings (exposure time = 100 ms, gain = 1) and merged with the images taken in light. The intensity of fluorescent images was calculated using NEOimage for FOBI (CELLGENTEK, Deajeon-si, Korea). Integrated density was quantified by multiplying area (number of pixels within the automatically designated region of interest [ROI]) with intensity unit (average of "intensity value/sec/gain" of each pixel within the region of interest [ROI]). Integrated density values in each timepoint were measured in a time-dependent manner in Figure 4G. Finally, the area under curves (AUC) was measured using PRISM software.

TEWL Analysis: The dorsal hair of C57BL/6 mice was shaved 24 h prior to the experiment. Assessments were conducted using a Tewameter (DermaLab combo, CORTEX TECHNOLOGY, Hadsund, Denmark) post-application. TEWL was measured before MN application and at 0.25, 0.5, 1, 2, 6, 12, and 24 h post-application in all mice.

Cell Culture: B16F10 (a murine melanoma cell line) was purchased from ATCC (Manassas, USA). Dulbecco's modified Eagle's medium (DMEM) supplemented with 1% penicillin-streptomycin (100 U/mL) and 10% fetal bovine serum (FBS) was used for B16F10 cell culture. The cells were incubated at 37°C in 5% CO_2 . All in vitro experiences were compared with non-treated B16F10 cells (Control).

Western Blot: Cells were lysed in RIPA buffer with a protease inhibitor cocktail and phosphatase inhibitor cocktail (Sigma-Aldrich) and centrifuged. Total cell lysates were resuspended in SDS sample buffer and resolved using SDS-PAGE. Proteins were transferred to Immobilon-P PVDF membrane (Sigma-Aldrich) and blocked with 5% bovine serum albumin (BSA)/TBST buffer for 1 h at room temperature. Membranes were incubated with primary antibodies overnight. Primary antibodies used for western blotting were anti-mouse E-cadherin (1:1000, Abcam, Boston, USA), anti-mouse N-cadherin (1:1000, Cell Signaling, Massachusetts, USA), anti-mouse Smad3 (1:1000, Abcam),

anti-mouse phospho-Smad3 (Ser423/425, 1:1000, Cell Signaling), and mouse anti-GAPDH (1:1000, Abcam). Next, membranes were incubated with secondary antibodies for 1 h at room temperature. Anti-rabbit HRP-linked antibody (1:2000, Cell Signaling) was used as the secondary antibody. The membranes were captured using ChemiDoc XRS+ (Bio-Rad, California, USA).

Wound Healing Assay: B16F10 cells were seeded at 5×10^4 cells/mL density, cultured in a 24-well plate, and incubated for 24 h at 37 °C with 5% CO₂. When cells were confluent, the wounds were scratched with the SPL SCAR Scratcher 24 well (SPL Life Sciences, Seoul, Korea) followed by a PBS washing to remove cell debris. The remaining adherent cells were treated with SD-208 (1 μM) and TGF-β (5 ng mL⁻¹). The scratches were captured using a microscope (OLYMPUS CKX41, Tokyo, Japan) and analyzed with ImageJ software using the following formula:

$$\text{Wound closure degree(\%)} = \frac{(\text{Initial wound area} - \text{Final wound area}) \times 100}{\text{Initial wound area}} \quad (1)$$

3D Spheroid Growth Assay: B16F10 cells were grown in culture conditions, harvested, and dissociated into single-cell suspensions for spheroid fabrication. Cells were seeded at a density of 1000 cells/100 μL in a PCR tube and centrifuged at 1200 rpm for 5 min to pellet the cells at the bottom of the tube. The cell pellets were incubated for 3 days at 37 °C in 5% CO₂ to fabricate spheroids. Incubated spheroids were transferred to ultra-low attachment (ULA) round-bottom 96-well plates (Corning, New York, USA) at 200 μL/well and incubated for 1 day at 37 °C in 5% CO₂ for spheroid stabilization. Stabilized spheroids were treated with SD-208 (1 μM) and TGF-β (5 ng mL⁻¹), incubated at 37 °C, and maintained with 50% medium replenishments every 3 days. Spheroids were captured using a microscope (OLYMPUS CKX41) and analyzed with ImageJ software.

In Vivo Immunotherapy of B16F10 Tumor-Bearing C57BL/6 Mice: Female C57BL/6 mice (6- to 7-week old) were kept in pathogen-free conditions with 12-h light/12-h dark cycles and free access to food and water. The subcutaneous melanoma mouse model was established by subcutaneous injection of 2×10^5 of B16F10 cells at the dorsal flank of C57BL/6 mice after the hair was shaved. When the volume of subcutaneous tumors reached 50–80 mm³, the mice were randomly divided into 6 groups (5 mice/group): PBS IT, (αPD-L1 Ab)/SD-208 IT (19.5 μg of αPD-L1 Ab and 45.5 μg of SD-208 per mouse), HA SLMN, (αPD-L1 Ab)/SD-208 SLMN, SD-208 SLMN, and αPD-L1 Ab SLMN. MN patches were applied to the tumor site for 1 min and further fixed using hydrocolloid patch for 2 h.

The tumor size in mice was evaluated by measuring the height and width of tumors using a digital caliper every 2 days. To ensure treatment safety, the weight of mice was monitored every 2 days. Mice were sacrificed when the tumor volume exceeded 2000 mm³. All animal experiments were conducted according to the protocol approved by the Institutional Animal Care and Use Committee of Hanyang University, registered as 2022-0035A.

Immunofluorescence Staining for Imaging of CD8⁺ and Granzyme B in the Tumor Microenvironment: Mouse tumors from different groups were harvested 8 days post-treatment. The harvested tumor samples were flash-frozen in OCT at -20 °C and sectioned using a cryostat to obtain 6-μm slices. The tumor sections were fixed with 100% ice-cold methanol or acetone, and permeabilization was conducted by incubating samples with PBS containing 0.1% Triton X-100 for 10 min. The tissues were washed with PBS and incubated with 1% bovine serum albumin (BSA) in PBS containing 0.1% Tween 20 (PBST) for 30 min to block the nonspecific binding of antibodies onto tumor cells. The sectioned samples were then stained with fluorescence-conjugated antibodies for Alexa 488-conjugated CD8 antibody (Santa Cruz, Dallas, USA) and Alexa 647-conjugated granzyme B antibody (Santa Cruz) at 4 °C overnight in the dark. Cell nuclei were counterstained with DAPI with a final concentration of 300 nM (BioLegend). Appropriate PBS washes were performed after each step. Following the standard immunofluorescence staining protocol, the tumor sections were mounted with Dako Fluorescence Mounting Medium. Fluorescence imaging was performed

using AxioScan.Z1 (Zeiss, Baden-Württemberg, Germany) and analyzed using ZEN 3.6 software.

TIL Assay: To assess the TILs, tumors were harvested at 8 days post-treatment and prepared into single-cell suspensions followed by removal of red blood cells using the RBC lysis buffer. Quantification of TILs was performed using flow cytometry (BD FACSCalibur, BD Biosciences, New Jersey, USA) via staining with anti-CD3-PE, anti-CD8a-PerCP, and anti-CD4-FITC antibodies.

Statistical Analysis: All the data were represented as the mean ± standard error of the mean (SEM). GraphPad Prism (version 8.02) for Windows (GraphPad Software) was used for statistical analysis. The difference between groups was compared by two-tailed *t*-test and comparisons among groups were performed using one-way ANOVA followed by Tukey's multiple comparisons test. All *p*-values < 0.05 were considered statistically significant (ns = non-significant, **p* < 0.033, ***p* < 0.02, ****p* < 0.01). Detailed processing of data and sample size for each analysis are described in the figure legends.

Supporting Information

Supporting Information is available from the Wiley Online Library or from the author.

Acknowledgements

This research was partially supported by grants from the National Research Foundation of Korea (NRF-2019R1A2C3008992); the Brain Korea 21 Fostering Outstanding Universities for Research (BK21 FOUR, 519990514440); the Korea Drug Development Fund funded by Ministry of Science and ICT, Ministry of Trade, Industry, and Energy, and Ministry of Health and Welfare (HN21C0885, Republic of Korea); and the Technology Development Program (S3303329) funded by the Ministry of SMEs and Startups (MSS, Korea).

Conflict of Interest

The authors declare no conflict of interest.

Data Availability Statement

The data that support the findings of this study are available from the corresponding author upon reasonable request.

Keywords

dissolvable microneedles, immunomodulation, melanoma immunotherapy, micro-stereolithography 3D printing, self-locking microneedles, transcutaneous drug delivery

Received: October 28, 2022

Revised: December 8, 2022

Published online:

[1] Y. Bao, N. Paunović, J.-C. Leroux, *Adv. Funct. Mater.* **2022**, *32*, 2109864.

[2] a) M. A. Ali, C. Hu, E. A. Yttri, R. Panat, *Adv. Funct. Mater.* **2022**, *32*, 2107671; b) Z. F. Rad, P. D. Prewett, G. J. Davies, *Microsyst. Nanoeng.* **2021**, *7*, 71.

- [3] J. dos Santos, R. S. de Oliveira, T. V. de Oliveira, M. C. Velho, M. V. Konrad, G. S. da Silva, M. Deon, R. C. R. Beck, *Adv. Funct. Mater.* **2021**, *31*, 2009691;
- [4] a) E. Larrañeta, R. E. M. Lutton, A. D. Woolfson, R. F. Donnelly, *Mater. Sci. Eng., R* **2016**, *104*, 1; b) S. Henry, D. V. McAllister, M. G. Allen, M. R. Prausnitz, *J. Pharm. Sci.* **1998**, *87*, 922; c) T. Waghule, G. Singhvi, S. K. Dubey, M. M. Pandey, G. Gupta, M. Singh, K. Dua, *Biomed. Pharmacother.* **2019**, *109*, 1249; d) H. L. Quinn, M. C. Kearney, A. J. Courtenay, M. T. McCrudden, R. F. Donnelly, *Expert Opin. Drug Delivery* **2014**, *11*, 1769.
- [5] S. M. Bal, A. C. Kruithof, R. Zwier, E. Dietz, J. A. Bouwstra, J. Lademann, M. C. Meinke, *J. Control. Release* **2010**, *147*, 218.
- [6] a) S. F. Lahiji, Y. Kim, G. Kang, S. Kim, S. Lee, H. Jung, *Sci. Rep.* **2019**, *9*, 7886; b) J. Chen, W. Huang, Z. Huang, S. Liu, Y. Ye, Q. Li, M. Huang, *AAPS PharmSciTech* **2018**, *19*, 1141.
- [7] a) S. F. Lahiji, M. Dangol, H. Jung, *Sci. Rep.* **2015**, *5*, 7914; b) S. Y. Yang, E. D. O'Carbhaill, G. C. Sisk, K. M. Park, W. K. Cho, M. Villiger, B. E. Bouma, B. Pomahac, J. M. Karp, *Nat. Commun.* **2013**, *4*, 1702; c) S. P. Davis, B. J. Landis, Z. H. Adams, M. G. Allen, M. R. Prausnitz, *J. Biomech.* **2004**, *37*, 1155; d) L. Y. Chu, M. R. Prausnitz, *J. Control. Release* **2011**, *149*, 242; e) M. C. Chen, S. F. Huang, K. Y. Lai, M. H. Ling, *Biomaterials* **2013**, *34*, 3077; f) X. Zhang, G. Chen, Y. Wang, L. Fan, Y. Zhao, *Adv. Sci.* **2022**, *9*, 2104883.
- [8] D. Schadendorf, A. C. J. van Akkooi, C. Berking, K. G. Griewank, R. Gutzmer, A. Hauschild, A. Stang, A. Roesch, S. Ugurel, *Lancet* **2018**, *392*, 971.
- [9] a) V. Gray-Schopfer, C. Wellbrock, R. Marais, *Nature* **2007**, *445*, 851; b) S. Kalaora, A. Nagler, J. A. Wargo, Y. Samuels, *Nat. Rev. Cancer* **2022**, *22*, 195.
- [10] M. Arnold, D. Singh, M. Laversanne, J. Vignat, S. Vaccarella, F. Meheus, A. E. Cust, E. de Vries, D. C. Whiteman, F. Bray, *JAMA Dermatol* **2022**, *158*, 495.
- [11] W. Guo, H. Wang, C. Li, *Signal Transduction Targeted Ther.* **2021**, *6*, 424.
- [12] a) R. J. Sullivan, K. T. Flaherty, *Nat. Rev. Clin. Oncol.* **2015**, *12*, 625; b) X. Zhang, C. Wang, J. Wang, Q. Hu, B. Langworthy, Y. Ye, W. Sun, J. Lin, T. Wang, J. Fine, H. Cheng, G. Dotti, P. Huang, Z. Gu, *Adv. Mater.* **2018**, *30*, 1707112.
- [13] a) J. Man, J. Millican, A. Mulvey, V. GebSKI, R. Hui, *JNCI Cancer Spectr.* **2021**, *5*, pkab012; b) I. Marquez-Rodas, P. Cerezuela, A. Soria, A. Berrocal, A. Riso, M. Gonzalez-Cao, S. Martin-Algarra, *Ann. Transl. Med.* **2015**, *3*, 267.
- [14] J. Kim, J. Hong, J. Lee, S. Fakhraei Lahiji, Y. H. Kim, *J. Control. Release* **2021**, *332*, 109.
- [15] a) M. K. Chan, J. Y. Chung, P. C. Tang, A. S. Chan, J. Y. Ho, T. P. Lin, J. Chen, K. T. Leung, K. F. To, H. Y. Lan, P. M. Tang, *Cancer Lett.* **2022**, *550*, 215925; b) D. Javelaud, L. van Kempen, V. I. Alexaki, E. L. Scolan, K. Luo, A. Mauviel, *Mol. Cancer* **2011**, *10*, 2.
- [16] M. T. Bu, P. Chandrasekhar, L. Ding, W. Hugo, *Pharmacol. Ther.* **2022**, *240*, 108211.
- [17] a) R. J. Akhurst, A. Hata, *Nat. Rev. Drug Discovery* **2012**, *11*, 790; b) S. Haque, J. C. Morris, *Hum. Vaccines Immunother.* **2017**, *13*, 1741.
- [18] a) D. Schmid, C. G. Park, C. A. Hartl, N. Subedi, A. N. Cartwright, R. B. Puerto, Y. Zheng, J. Maiarana, G. J. Freeman, K. W. Wucherpfennig, D. J. Irvine, M. S. Goldberg, *Nat. Commun.* **2017**, *8*, 1747; b) K. S. Mohammad, D. Javelaud, P. G. Fournier, M. Niewolna, C. R. McKenna, X. H. Peng, V. Duong, L. K. Dunn, A. Mauviel, T. A. Guise, *Cancer Res.* **2011**, *71*, 175.
- [19] G. Yin, W. Guo, H. Liu, Z. Huang, X. Chen, *Curr. Probl. Cancer* **2022**, *46*, 100878.
- [20] a) Y. Hao, D. Baker, P. T. Dijke, *Int. J. Mol. Sci.* **2019**, *20*, 2767; b) P. Papageorgis, *J. Oncol.* **2015**, *2015*, 587193.
- [21] B. O. Sun, Y. Fang, Z. Li, Z. Chen, J. Xiang, *Biomed. Rep.* **2015**, *3*, 603.
- [22] J. Winkler, A. Abisoye-Ogunniyan, K. J. Metcalf, Z. Werb, *Nat. Commun.* **2020**, *11*, 5120.
- [23] D. R. Principe, J. A. Doll, J. Bauer, B. Jung, H. G. Munshi, L. Bartholin, B. Pasche, C. Lee, P. J. Grippo, *J. Natl. Cancer Inst.* **2014**, *106*, djt369.
- [24] C. Y. Loh, J. Y. Chai, T. F. Tang, W. F. Wong, G. Sethi, M. K. Shanmugam, P. P. Chong, C. Y. Looi, *Cells* **2019**, *8*, 1118.
- [25] a) M. Stadler, M. Scherzer, S. Walter, S. Holzner, K. Pudelko, A. Riedl, C. Unger, N. Kramer, B. Weil, J. Neesen, M. Hengstschlager, H. Dolznig, *Sci. Rep.* **2018**, *8*, 1151; b) M. Schmidt, C. J. Scholz, C. Polednik, J. Roller, *Oncol. Rep.* **2016**, *35*, 2431.
- [26] M. Yi, M. Niu, L. Xu, S. Luo, K. Wu, *J. Hematol. Oncol.* **2021**, *14*, 10.
- [27] A. Akinleye, Z. Rasool, *J. Hematol. Oncol.* **2019**, *12*, 92.
- [28] S. Oguchi, T. Saida, Y. Koganehira, S. Ohkubo, Y. Ishihara, S. Kawachi, *Arch. Dermatol.* **1998**, *134*, 563.
- [29] S. P. Cullen, M. Brunet, S. J. Martin, *Cell Death Differ.* **2010**, *17*, 616.
- [30] H. Raskov, A. Orhan, J. P. Christensen, I. Gogenur, *Br. J. Cancer* **2021**, *124*, 359.